J. Fluid Mech. (2022), *vol*. 952, R1, doi:10.1017/jfm.2022.906

Turbulent Prandtl number from isotropically forced turbulence

Petri J. Käpylä[1],† **and Nishant K. Singh**[2]

[1]Institute for Astrophysics and Geophysics, Göttingen University, Friedrich-Hund-Platz 1, 37077 Göttingen, Germany

[2]Inter-University Centre for Astronomy and Astrophysics, Post Bag 4 Ganeshkhind, Savitribai Phule Pune University Campus, Pune 411 007, India

(Received 21 July 2022; revised 30 September 2022; accepted 15 October 2022)

Turbulent motions enhance the diffusion of large-scale flows and temperature gradients. Such diffusion is often parameterized by coefficients of turbulent viscosity (ν_t) and turbulent thermal diffusivity (χ_t) that are analogous to their microscopic counterparts. We compute the turbulent diffusion coefficients by imposing sinusoidal large-scale velocity and temperature gradients on a turbulent flow and measuring the response of the system. We also confirm our results using experiments where the imposed gradients are allowed to decay. To achieve this, we use weakly compressible three-dimensional hydrodynamic simulations of isotropically forced homogeneous turbulence. We find that the turbulent viscosity and thermal diffusion, as well as their ratio the turbulent Prandtl number, $Pr_t = \nu_t/\chi_t$, approach asymptotic values at sufficiently high Reynolds and Péclet numbers. We also do not find a significant dependence of Pr_t on the microscopic Prandtl number $Pr = \nu/\chi$. These findings are in stark contrast to results from the $k{-}\epsilon$ model, which suggests that Pr_t increases monotonically with decreasing Pr. The current results are relevant for the ongoing debate on, for example, the nature of the turbulent flows in the very-low-Pr regimes of stellar convection zones.

Key words: turbulence simulation, homogeneous turbulence, turbulent mixing

1. Introduction

The fluids in stellar convection zones are generally characterized by a low microscopic Prandtl number, $Pr = \nu/\chi$, where ν is the kinematic viscosity and χ is the thermal diffusivity (e.g. Ossendrijver 2003; Augustson, Brun & Toomre 2019). Typical values

† Email address for correspondence: pkaepyl@uni-goettingen.de

in the bulk of the solar convection zone, for example, range between 10^{-6} and 10^{-3} (Schumacher & Sreenivasan 2020). Recently, several studies have explored the possibility that solar convection operates at a high effective Prandtl number regime, meaning that the turbulent Prandtl number Pr_t exceeds unity (e.g. O'Mara *et al.* 2016; Bekki, Hotta & Yokoyama 2017; Karak, Miesch & Bekki 2018), as a possible solution to the too high velocity amplitudes in simulations in comparison to the Sun (e.g. Hanasoge, Duvall & Sreenivasan 2012; Schumacher & Sreenivasan 2020). However, few attempts have been made to actually measure the turbulent Prandtl number from simulations. A notable exception is the study of Pandey, Schumacher & Sreenivasan (2021), who reported that the turbulent Prandtl number decreases steeply as a function of the molecular Prandtl number, so that $Pr_t \propto Pr^{-1}$ in simulations of standard Boussinesq and variable-heat-conductivity Boussinesq convection. Similar results have recently been reported by Tai *et al.* (2021) and Pandey *et al.* (2022*a*).

The difficulty in measuring turbulent diffusivities in the absence of large-scale gradients has led to the development of combined eddy-diffusivity mass-flux approaches in convective boundary layers (Siebesma, Soares & Teixeira 2007). Here we instead set out to measure turbulent viscosity and thermal diffusivity from a simpler system of isotropically forced homogeneous turbulence. This is done by imposing large-scale gradients of velocity and temperature (equivalently specific entropy) and measuring the response of the system. The turbulent diffusion coefficients are computed from the Boussinesq ansatz and an analogous expression for the enthalpy flux. This method provides a direct measurement of the diffusion coefficients without the need to resort to turbulent closures. Similar methods were used recently to measure the turbulent magnetic Prandtl number (Käpylä *et al.* 2020). We compare our results with those from the widely used k–ϵ model, which was also used by Pandey *et al.* (2021). We show that the direct results and those from the k–ϵ model are systematically different and that the latter yields misleading results in the flows studied here.

2. The model

We model isotropically forced, non-isothermal turbulence in a fully periodic cube of volume $(2\pi)^3$. We solve the equations of fully compressible hydrodynamics

$$\frac{\mathrm{D}\ln\rho}{\mathrm{D}t} = -\boldsymbol{\nabla}\cdot\boldsymbol{u}, \tag{2.1}$$

$$\frac{\mathrm{D}\boldsymbol{u}}{\mathrm{D}t} = -\frac{1}{\rho}(\boldsymbol{\nabla}p - \boldsymbol{\nabla}\cdot 2\nu\rho\boldsymbol{\mathcal{S}}) + \boldsymbol{f} - \frac{1}{\tau}(\boldsymbol{u}-\bar{\boldsymbol{u}}_0), \tag{2.2}$$

$$T\frac{\mathrm{D}s}{\mathrm{D}t} = -\frac{1}{\rho}(\boldsymbol{\nabla}\cdot\boldsymbol{\mathcal{F}}_{rad} - \mathcal{C}) + 2\nu\boldsymbol{\mathcal{S}}^2 - \frac{T}{\tau}(s-\bar{s}_0), \tag{2.3}$$

where $\mathrm{D}/\mathrm{D}t = \partial/\partial t + \boldsymbol{u}\cdot\boldsymbol{\nabla}$ is the advective derivative, ρ is the density, $\boldsymbol{u}$ is the velocity, p is the pressure, ν is the kinematic viscosity, $\boldsymbol{\mathcal{S}}$ is the traceless rate-of-strain tensor with

$$\mathcal{S}_{ij} = \tfrac{1}{2}(u_{i,j}+u_{j,i}) - \tfrac{1}{3}\delta_{ij}\boldsymbol{\nabla}\cdot\boldsymbol{u}, \tag{2.4}$$

$\boldsymbol{f}$ is the external forcing, τ is a relaxation timescale and $\bar{\boldsymbol{u}}_0$ is the target mean velocity profile. Furthermore, T is the temperature, s is the specific entropy, $\boldsymbol{\mathcal{F}}_{rad}$ is the radiative flux, $\mathcal{C}$ is a cooling term and $\bar{s}_0$ is the target mean specific entropy profile. Radiation is

modelled via the diffusion approximation, with the radiative flux given by

$$\boldsymbol{\mathcal{F}}_{rad} = -c_P \rho \chi \boldsymbol{\nabla} T, \tag{2.5}$$

where c_P is the specific heat in constant pressure and χ is the thermal diffusivity. The ideal gas equation of state $p = (c_P - c_V)\rho T = \mathcal{R}\rho T$ is assumed, where $\mathcal{R}$ is the gas constant and c_V is the specific heat capacity at constant volume. In a non-isothermal system with forcing and/or imposed large-scale flow, viscous dissipation of kinetic energy acts as a source for thermal energy and leads to a linear increase of the temperature. Additional volumetric cooling is applied to counter this with

$$\mathcal{C}(\boldsymbol{x}) = \rho c_P \frac{T(\boldsymbol{x}) - \langle T_0 \rangle}{\tau_{cool}}, \tag{2.6}$$

where $\langle T_0 \rangle$ is the volume-averaged initial temperature and τ_{cool} is a cooling timescale. We use $\tau = \tau_{cool} = (c_{s0} k_1)^{-1}$, where c_{s0} is the initial uniform value of the sound speed and k_1 is the wavenumber corresponding to the box scale.

The external forcing is given by

$$\boldsymbol{f} = \mathrm{Re}\{N(t) \boldsymbol{f}_{\boldsymbol{k}(t)} \exp[\mathrm{i}\boldsymbol{k}(t) \cdot \boldsymbol{x} - \mathrm{i}\phi(t)]\} \tag{2.7}$$

(see Brandenburg 2001), where $\boldsymbol{x}$ is the position vector and $N(t) = f_0 c_s (k(t) c_s / \delta t)^{1/2}$ is a normalization factor in which f_0 is the forcing amplitude, $k = |\boldsymbol{k}|$, δt is the length of the time step, and $-\pi < \phi(t) < \pi$ is a random delta-correlated phase. The vector $\boldsymbol{f}_{\boldsymbol{k}}$ describes non-helical transverse waves and is given by

$$\boldsymbol{f}_{\boldsymbol{k}} = \frac{\boldsymbol{k} \times \hat{\boldsymbol{e}}}{\sqrt{\boldsymbol{k}^2 - (\boldsymbol{k} \cdot \hat{\boldsymbol{e}})^2}}, \tag{2.8}$$

where $\hat{\boldsymbol{e}}$ is an arbitrary unit vector, and where the wavenumber $\boldsymbol{k}$ is randomly chosen. The target profiles of mean velocity and specific entropy are given by

$$\bar{\boldsymbol{u}}_0 = u_0 \sin(k_1 z) \hat{\boldsymbol{e}}_y, \tag{2.9}$$

$$\bar{s}_0 = s_0 \sin(k_1 z). \tag{2.10}$$

The imposed mean flow is sufficiently weak so that the turbulence remains nearly isotropic and turbulence production due to the shear is negligible. In addition to the physical diffusion, the advective terms in (2.1) to (2.3) are implemented in terms of fifth-order upwinding derivatives with sixth-order hyperdiffusive corrections and flow-dependent diffusion coefficients; see appendix B of Dobler, Stix & Brandenburg (2006).

The PENCIL CODE (Pencil Code Collaboration *et al.* 2021) (http://github.com/pencil-code), which uses high-order finite differences for spatial and temporal discretization, was used to produce the numerical simulations.

2.1. *Units, system parameters and diagnostics*

The equations are non-dimensionalized by choosing the units

$$[x] = k_1^{-1}, \quad [\rho] = \rho_0, \quad [u] = c_{s0}, \quad [s] = c_P, \tag{2.11a–d}$$

where ρ_0 is the initial uniform density and $c_{s0} = \sqrt{\gamma \mathcal{R} T_0}$ is the sound speed corresponding to the initial temperature T_0. The level of velocity fluctuations is determined

by the forcing amplitude f_0 along with the kinematic viscosity. A key system parameter is the ratio of kinematic viscosity and thermal diffusion or the Prandtl number

$$Pr = \frac{\nu}{\chi}, \tag{2.12}$$

which is varied between 0.01 and 10 in the present study. The Reynolds and Péclet numbers quantify the level of turbulence of the flows:

$$Re = \frac{u_{rms}}{\nu k_f}, \quad Pe = PrRe = \frac{u_{rms}}{\chi k_f}, \tag{2.13a,b}$$

where $u_{rms} = \sqrt{\langle (\boldsymbol{u} - \bar{\boldsymbol{u}}_0)^2 \rangle}$ is the volume-averaged fluctuating root mean square velocity and k_f is the average forcing wavenumber characterizing the energy injection scale. The latter is chosen from a uniformly distributed narrow range in the vicinity of $5k_1$. The imposed gradients of large-scale flow and entropy are quantified by

$$Ma_s = \frac{u_0}{c_{s0}}, \quad Ma_g = \frac{[(\gamma - 1)s_0 T_0]^{1/2}}{c_{s0}}, \tag{2.14a,b}$$

where Ma_s is the Mach number of the mean flow. The Mach number of the turbulent flow is given by

$$Ma = \frac{u_{rms}}{\langle c_s \rangle}, \tag{2.15}$$

where $\langle c_s \rangle$ is the volume-averaged speed of sound.

Mean values are taken to be horizontal averages denoted by bars; that is,

$$\bar{f} = \frac{1}{(2\pi)^2} \int_x \int_y f(\boldsymbol{x}) \, \mathrm{d}x \, \mathrm{d}y. \tag{2.16}$$

Often an additional time average over the statistically steady part of the simulation is taken. Volume averages are denoted by angle brackets $\langle . \rangle$, apart from the root mean square values, which are always assumed to be volume-averaged unless otherwise stated. Errors were estimated by dividing the time series into three parts and averaging over each subinterval. The greatest deviation from the average computed over the whole time series was taken as the error estimate.

3. Results

The simulations discussed in the present study are listed in table 1.

3.1. *Turbulent viscosity and heat diffusion from imposed flow and entropy methods*

We measure the turbulent viscosity and thermal diffusivity using large-scale gradients of $\boldsymbol{u}$ and s in two ways. First, we impose sinusoidal large-scale profiles of velocity (2.9) or entropy (2.10). The response of the system consists of non-zero Reynolds stress and vertical enthalpy flux profiles that are parameterized with gradient diffusion terms

Set	Pr	Re	Pe	Ma	Ma_s	Ma_g	#runs
i001	0.01	27 . . . 779	0.27 . . . 7.8	0.069 . . . 0.079	0.01 . . . 0.03	0.07 . . . 0.1	10
i002	0.02	27 . . . 779	0.54 . . . 16	0.069 . . . 0.080	0.01 . . . 0.03	0.07 . . . 0.1	12
i005	0.05	27 . . . 780	1.4 . . . 39	0.069 . . . 0.080	0.01 . . . 0.03	0.07 . . . 0.1	12
i010	0.1	12 . . . 800	1.2 . . . 80	0.060 . . . 0.082	0.01 . . . 0.03	0.07 . . . 0.1	30
i020	0.2	27 . . . 781	5.4 . . . 156	0.069 . . . 0.080	0.01 . . . 0.03	0.07 . . . 0.1	10
i025	0.25	397	99	0.081	0.01 . . . 0.03	0.07 . . . 0.1	2
i050	0.5	27 . . . 781	14 . . . 390	0.069 . . . 0.081	0.01 . . . 0.03	0.07 . . . 0.1	12
i075	0.75	399	301	0.081	0.01 . . . 0.03	0.07 . . . 0.1	2
i100	1.0	27 . . . 1582	27 . . . 1582	0.069 . . . 0.081	0.01 . . . 0.03	0.07 . . . 0.1	14
i200	2.0	22	44	0.068	0.01 . . . 0.03	0.07 . . . 0.1	2
i500	5.0	22.2	111	0.068	0.01 . . . 0.03	0.07 . . . 0.1	2
i1000	10.0	22.3	223	0.068	0.01 . . . 0.03	0.07 . . . 0.1	2
du001	0.01	153	1.5	0.078	0.01	—	10
du010	0.1	153 . . . 391	15 . . . 39	0.078	0.01 . . . 0.03	—	11
du100a	1.0	154	154	0.079	0.01	—	10
du100b	1.0	154	154	0.079	0.03	—	10
ds001	0.01	153	1.5	0.078	—	0.1	10
ds010	0.1	153 . . . 391	15 . . . 39	0.078	—	0.07 . . . 0.1	11
ds100	1.0	153	153	0.078	—	0.1	10

Table 1. Summary of runs. Runs with imposed velocity or specific entropy gradients are denoted by the prefix i, whereas decay experiments of velocity (specific entropy) are identified by the prefix du (ds). Grid resolutions range between 144^3 and 1152^3.

(e.g. Rüdiger 1989),

$$F_z^{enth}(z) = c_P\overline{(\rho u_z)'T'} \approx c_P\bar{\rho}\overline{u_z'T'} = -\chi_t\bar{\rho}\bar{T}\frac{\partial\bar{s}}{\partial z} \tag{3.1}$$

and

$$R_{yz}(z) = \overline{u_y'u_z'} = -\nu_t\frac{\partial\bar{u}_y}{\partial z}, \tag{3.2}$$

where primes denote fluctuations from the mean, e.g. $\boldsymbol{u}' = \boldsymbol{u} - \bar{\boldsymbol{u}}$. The Mach number in the current simulations is always less than 0.1. Therefore we neglect density-dependent terms in our analysis, because they scale with Ma^2.

The coefficients χ_t and ν_t are assumed to be scalars and were obtained from linear fits between time-averaged F_z^{enth} and $-\bar{\rho}\bar{T}\partial_z\bar{s}$ and between R_{yz} and $-\partial_z\bar{u}_y$, respectively. Results from our simulations are shown in figure 1. We normalize ν_t and χ_t by

$$\nu_{t0} = \chi_{t0} = \tfrac{1}{3}u_{rms}k_f^{-1}, \tag{3.3}$$

which is an order-of-magnitude estimate for the turbulent diffusion coefficients. We note that in the parameter regimes studied here, the estimates ν_{t0} and χ_{t0} are very similar in all of our runs. Our results show that for low Péclet numbers the turbulent heat diffusion increases in proportion to Pe for $Pe \lesssim 1$. This is consistent with earlier numerical results for turbulent viscosity (e.g. Käpylä *et al.* 2020), magnetic diffusivity (e.g. Sur, Brandenburg & Subramanian 2008) and passive scalar diffusion (Brandenburg, Svedin & Vasil 2009), and with corresponding analytic results in the diffusion-dominated ($Pe \ll 1$) regime. For sufficiently large Pe, $\tilde{\chi}_t$ tends to a constant value. The turbulent viscosity is

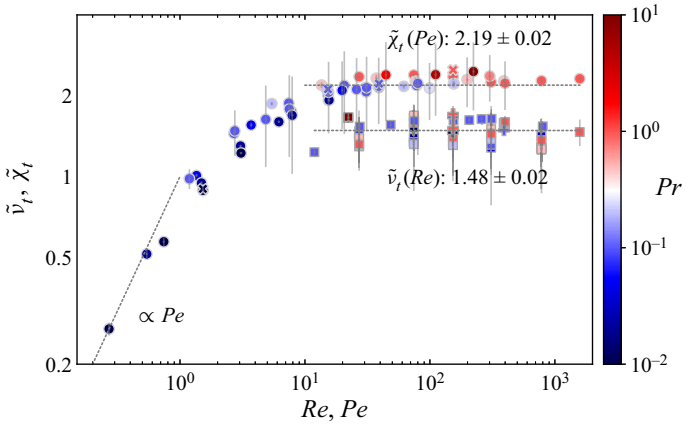

Figure 1. Normalized turbulent viscosity $\tilde{\nu}_t = \nu_t/\nu_{t0}$ (squares) and heat diffusivity $\tilde{\chi}_t = \chi_t/\chi_{t0}$ (circles) as functions of Reynolds and Péclet numbers. The crosses ($\times$) and pluses ($+$) indicate results from decay experiments. The colours of the symbols indicate the microscopic Prandtl number as shown by the colour bar. The dotted horizontal lines show fit to the data for $Pe, Re > 10$, and a line proportional to Pe is shown for low Pe.

also roughly constant in the parameter space covered here. For low fluid Reynolds numbers ν_t is proportional to Re, as has been shown in Käpylä *et al.* (2020). However, we do not cover this parameter regime with the current simulations.

3.2. *Turbulent viscosity and heat diffusion from decay experiments*

The second approach to computing ν_t and χ_t relies on the decay of the imposed gradients of $\bar{\boldsymbol{u}}$ and $\bar{s}$. This is an independent way to measure turbulent viscosity and heat diffusion. Snapshots from the imposed velocity/entropy gradient runs were used as initial conditions, and the relaxation terms of the right-hand sides of the Navier–Stokes and entropy equations were deactivated. The large-scale velocity and entropy profiles in such runs decay because of the combined effect of molecular and turbulent diffusion. To measure the decay rate we monitored the amplitude of the $k = k_1$ components of $\bar{u}_y$ and $\bar{s}$. Exponential decay laws

$$\bar{u}_y(t, k_1) = \bar{u}_y(t_0, k_1)\exp(-(\nu_t + \nu)t), \quad \bar{s}(t, k_1) = \bar{s}(t_0, k_1)\exp(-(\chi_t + \chi)t) \quad (3.4a,b)$$

were then fitted to the numerical data. Representative examples from decay experiments of large-scale velocity and entropy are shown in figure 2. The upper panels (a,b) show $\bar{u}_y(z, t)$ and $\bar{s}_y(z, t)$ from typical decay experiments. The k_1 components of these fields decay exponentially when the forcing is turned off; see panels (c,d) of figure 2. Ultimately the amplitude of the k_1 mode decreases sufficiently so that it cannot be distinguished from the background turbulence. The time it takes to reach this state varies and depends on the initial amplitudes u_0 and s_0. However, at the same time, these amplitudes need to be kept as low as possible to prevent nonlinear effects from becoming important (see e.g. Käpylä *et al.* 2020). This is particularly important for the velocity field, because of which the range from which turbulent viscosity can be estimated is limited, which necessitates running several experiments with different snapshots as initial conditions to reach converged values for ν_t and χ_t.

For this reason, only a limited subset of the parameter range covered by the imposed cases were repeated with decay experiments. We used ten snapshots from each run for the decay experiments. The separation between the snapshots is roughly $\Delta t = 40 u_{rms} k_f$, so

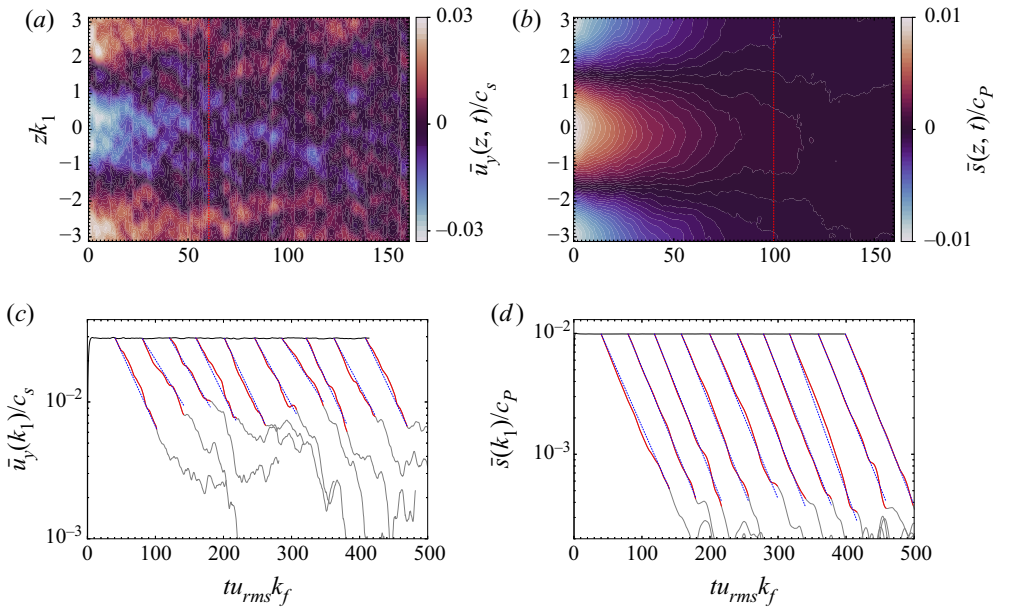

Figure 2. Panels (*a*,*b*) show $\bar{u}_y(t,z)$ and $\bar{s}(t,z)$ normalized by c_s and c_P, respectively, from decay experiments with $Pr = 1$ and $Re = 157$. Red vertical lines denote end times of exponential fits. Panels (*c*,*d*) show temporal decays of the $k_z/k_1 = 1$ mode of $\bar{u}_y$ and $\bar{s}$, respectively; the black line shows the progenitor run, and the red/grey lines indicate the decaying runs. The red part is used to fit exponential decay; the blue dotted lines show the exponential fit.

that the realizations can be considered uncorrelated. Results from the decay experiments are shown in figure 1 with crosses (χ_t) and pluses (ν_t). We find that the results from the decay experiments are consistent with those from the imposed flow and entropy gradient methods.

3.3. *The $k-\epsilon$ model*

To facilitate a comparison with Pandey *et al.* (2021), we use the expressions for ν_t and χ_t derived under the $k-\epsilon$ model with

$$\nu_t^{(k-\epsilon)} = c_\nu' k_u^2/\epsilon_K, \tag{3.5}$$

$$\chi_t^{(k-\epsilon)} = c_\chi' k_u k_T/\epsilon_T, \tag{3.6}$$

where $k_u = \langle \boldsymbol{u}'^2\rangle/2$ is the turbulent kinetic energy, $k_T = \langle T'^2\rangle$ is the variance of the temperature fluctuations, and c_ν' and c_χ' are assumed to be universal constants. (The primes indicate the constancy of c_ν' and c_χ'; however, see also § 3.4, where this assumption is lifted.) The viscous and thermal dissipation rates are defined as $\epsilon_K = 2\nu[\langle \boldsymbol{S}^2\rangle - \langle \boldsymbol{S}_0^2\rangle]$ and $\epsilon_T = \chi\langle(\boldsymbol{\nabla} T')^2\rangle = \chi[\langle(\boldsymbol{\nabla} T)^2\rangle - \langle(\boldsymbol{\nabla}\bar{T})^2\rangle]$, respectively, where we have removed contributions from the mean flow and the mean entropy; $\boldsymbol{S}_0$ denotes the traceless rate-of-strain tensor as defined in (2.4) but with $\bar{\boldsymbol{u}}_0$ instead of $\boldsymbol{u}$. Pandey *et al.* (2021) computed Pr_t using the $k-\epsilon$ model by fixing the ratio c_ν'/c_χ', which yields

$$Pr_t^{(k-\epsilon)} = \frac{\nu_t^{(k-\epsilon)}}{\chi_t^{(k-\epsilon)}} = \frac{c_\nu'}{c_\chi'}\frac{k_u\epsilon_T}{k_T\epsilon_u}. \tag{3.7}$$

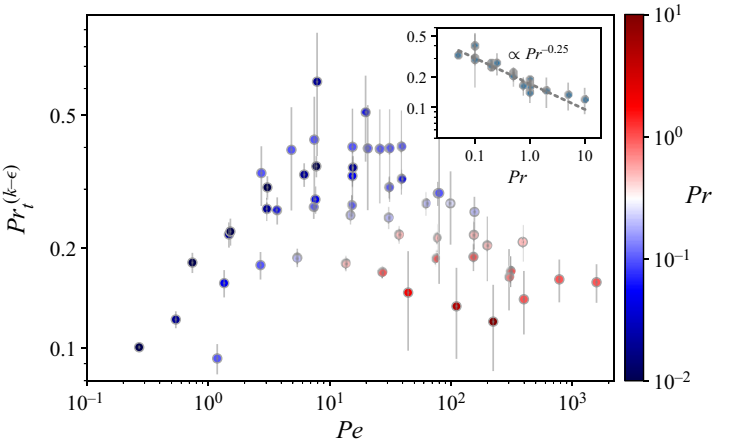

Figure 3. Turbulent Prandtl number $Pr_t^{(k-\epsilon)}$ according to (3.7) as a function of Péclet number. The colour of the symbols denotes the molecular Prandtl number as indicated by the colour bar. Inset: $Pr_t^{(k-\epsilon)}$ versus Pr from runs with $Pe > 20$.

For simplicity, we assume $c'_\nu/c'_\chi = 1$ in this subsection. The results are shown in figure 3. We find that taking the ratio c'_ν/c'_χ to be a constant leads to results where $Pr_t^{(k-\epsilon)}$ increases monotonically with decreasing Pr when Pe is larger than about 20; see the inset in figure 3, which reveals a dependence of $Pr^{-0.25}$. Qualitatively, this result is in agreement with the one in Pandey *et al.* (2021). However, we would like to note here that a strong assumption was made to reach this conclusion, namely, that the ratio c'_ν/c'_χ is fixed, and that c'_ν and c'_χ are universal constants, independent of control parameters such as Re and Pe. Henceforth, we relax these assumptions, and also omit primes from the coefficients c_ν and c_χ.

3.4. *Relaxing the assumption that c_ν and c_χ are constants*

It is reasonable to assume that for sufficiently large Reynolds and Péclet numbers, k_u and k_T tend to constant values. Furthermore, there is evidence from numerical simulations that ϵ_K, normalized by u_{rms}^3/ℓ where $\ell = 2\pi/k_f$, also tends to a non-zero constant value for large Reynolds numbers; see e.g. Frisch (1995) and Pandey *et al.* (2022*b*). Similar evidence for ϵ_T has not been presented. Therefore it is not clear whether the assumption of universality of c_ν and c_χ is valid. This is particularly important for numerical simulations, such as those in the current study, where the Reynolds and Péclet numbers are still modest. Since we have independently measured ν_t and χ_t using the imposed flow and entropy method (§ 3.1) and from decay experiments (§ 3.2), we can estimate c_ν and c_χ using

$$c_\nu = \nu_t/(k_u^2/\epsilon_K), \tag{3.8}$$

$$c_\chi = \chi_t/(k_u k_T/\epsilon_T), \tag{3.9}$$

where ν_t and χ_t are the ones obtained above in § 3.1 with the imposed field method. The results are shown in figure 4. They indicate that c_ν and c_χ are highly variable and that they depend not only on Re and Pe but also on Pr. Furthermore, for sufficiently large Reynolds and Péclet numbers, c_ν and c_χ show decreasing trends proportional to roughly the -0.25 power of Re and Pe, respectively. This shows that any estimate of ν_t or χ_t with the $k{-}\epsilon$ model in the parameter regime studied here would require prior knowledge of c_ν and c_χ for the particular parameters (Re, Pe, Pr) of that system.

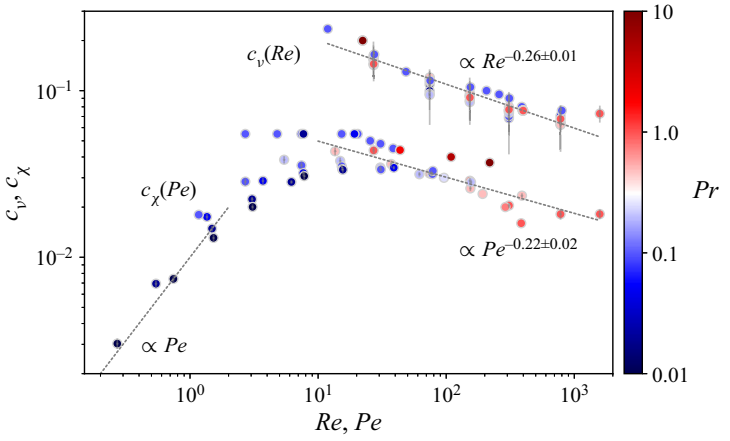

Figure 4. Similar to figure 1 but for $c_\nu(Re)$ and $c_\kappa(Pe)$ from (3.8) and (3.9). The colours again indicate the microscopic Prandtl number. The grey dotted lines indicate fits to the data for $(Pe, Re > 10)$, and a line proportional to Pe is shown for low Pe.

3.5. *Turbulent Prandtl number*

Our results for the turbulent Prandtl number

$$Pr_t = \frac{\nu_t}{\chi_t} \tag{3.10}$$

are shown in figure 5 with ν_t and χ_t as discussed in §§ 3.1 and 3.2. The data fall into a smooth sequence as a function of the Péclet number in the parameter regime studied here, where the turbulent viscosity is not strongly dependent on Re; see figure 5. We find that for $Pe \lesssim 1$ the turbulent Prandtl number is roughly inversely proportional to Pe for low molecular Prandtl number. We have not computed the turbulent Prandtl number for cases where both Re and Pe are smaller than unity. For sufficiently high Péclet number the turbulent Prandtl number tends to a constant value which is close to 0.7. This is in accordance with theoretical estimates, in that Pr_t is somewhat smaller than unity. For example, Rüdiger (1989) derived $Pr_t = 2/5$ using a first-order smoothing approximation. The turbulent Prandtl number also plays an important role in the atmospheric boundary layer, where several methods yield values of the order of unity (Li 2019, and references therein). The data for Pr_t show much stronger scatter when plotted as a function of Pr or Re; see figure 6. The scatter is due to the dependence of χ_t on the Péclet number at low Pe.

The fact that the turbulent Prandtl number Pr_t reaches a constant value at sufficiently large Pe, independent of Pr, is in stark contrast to the results obtained from the $k{-}\epsilon$ model with a fixed c_ν/c_χ; compare figures 3 and 5. Now we make an attempt to understand the reason for this discrepancy. From figure 4 we note the following approximate scaling relations at sufficiently large Re and Pe: $c_\nu \propto Re^{-0.25}$ and $c_\chi \propto Pe^{-0.25}$, which suggests that the ratio c_ν/c_χ scales with the Prandtl number as $Pr^{+0.25}$. With this, if we let $c'_\nu/c'_\chi \propto Pr^{+0.25}$ in (3.7), instead of a fixed ratio, and note from the inset of figure 3 that the factor $k_u\epsilon_T/k_T\epsilon_u \propto Pr^{-0.25}$, we would obtain from (3.7) that $Pr_t^{(k-\epsilon)}$ becomes independent of Pr, which agrees qualitatively with our results as shown in figure 5. Therefore we conclude that the results from the $k{-}\epsilon$ model with a fixed value for the ratio c_ν/c_χ are unreliable in the present flows. We note that the strong dependence of Pr_t on Pr found in Pandey *et al.* (2021) with the $k{-}\epsilon$ model has also been found using the gradient method in

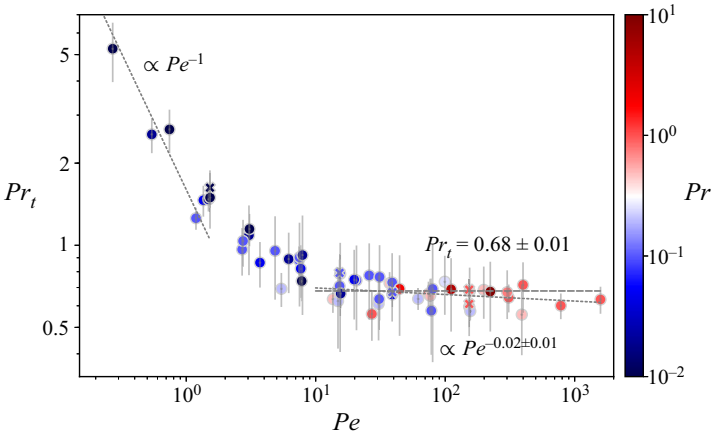

Figure 5. Turbulent Prandtl number $Pr_t = \nu_t/\chi_t$ as a function of Péclet number. The colour of the symbols denotes the molecular Prandtl number as indicated by the colour bar. The crosses (×) show results from decay experiments. Linear and power law fits to data for $Pe > 10$ are shown by the dashed and dotted lines, respectively, and a line proportional to Pe^{-1} is shown for low Pe.

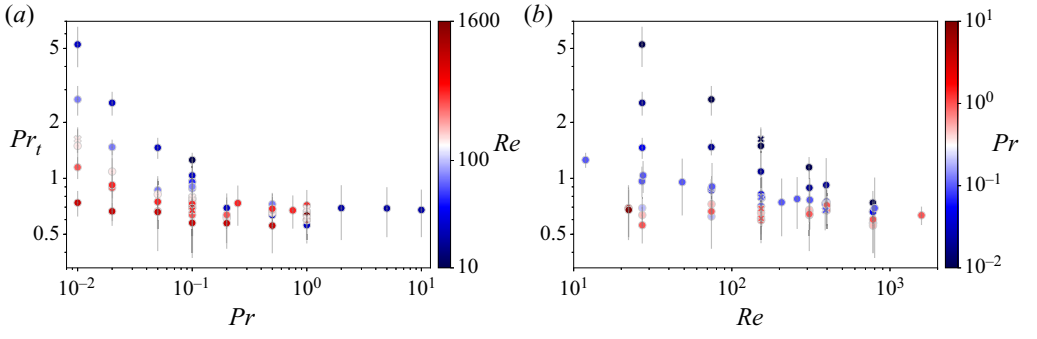

Figure 6. Turbulent Prandtl number Pr_t as a function of (*a*) Pr and (*b*) Re; crosses (×) show results from decay experiments.

Tai *et al.* (2021) and Pandey *et al.* (2022*a*). This suggests that the behaviour of $Pr_t(Pr)$ found by these authors is not specific to the $k-\epsilon$ model in that case but reflects the properties of Boussinesq convection at constant Rayleigh number.

4. Conclusions

Using simulations of weakly compressible isotropically forced turbulence with imposed large-scale gradients of velocity and temperature, and corresponding decay experiments, we find that the turbulent Prandtl number Pr_t is roughly 0.7 and is independent of the microscopic Prandtl number Pr provided that the Péclet number is higher than about 10. This is in contrast to the recent results of Pandey *et al.* (2021), who found that $Pr_t \propto Pr^{-1}$ from non-Boussinesq simulations of convection using the $k-\epsilon$ model. Although the physical set-ups are quite different, we were able to qualitatively reproduce their finding under the assumption that c_ν/c_χ is fixed. However, given that these results differ qualitatively from those obtained from the imposed gradient method and decay experiments, the former results are considered unreliable for the system under

consideration here. The fact that the gradient method yields a similar Pr dependence as the $k-\epsilon$ model for Boussinesq convection (Tai *et al.* 2021; Pandey *et al.* 2022*a*) suggests that in those flows the behaviour of turbulent transport can indeed be different. This is possibly connected to the strong driving of flows in the low-Pr regime when the Rayleigh number is fixed (e.g. Spiegel 1962). This issue will be addressed in a future study.

Acknowledgements. We thank an anonymous referee and K. Sreenivasan for their comments and suggestions. We thank S. Sridhar for his comments on an earlier draft of the manuscript. N.S. thanks the hospitality provided by RRI, Bangalore, where parts of this work were done. We gratefully acknowledge the use of high-performance computing facilities at HLRN in Göttingen and Berlin, and at IUCAA, Pune.

Funding. This work was supported by the Deutsche Forschungsgemeinschaft Heisenberg programme (P.J.K., grant number KA4825/4-1).

Declaration of interests. The authors report no conflict of interest.

Author ORCIDs.
Petri J. Käpylä https://orcid.org/0000-0001-9619-0053;
Nishant K. Singh https://orcid.org/0000-0001-6097-688X.

Author contributions. Both authors contributed equally to running the simulations, analysing data, reaching conclusions, and writing the paper.

References

Augustson, K.C., Brun, A.S. & Toomre, J. 2019 Rossby and magnetic Prandtl number scaling of stellar dynamos. *Astrophys. J.* **876** (1), 83.

Bekki, Y., Hotta, H. & Yokoyama, T. 2017 Convective velocity suppression via the enhancement of the subadiabatic layer: role of the effective Prandtl number. *Astrophys. J.* **851**, 74.

Brandenburg, A. 2001 The inverse cascade and nonlinear alpha-effect in simulations of isotropic helical hydromagnetic turbulence. *Astrophys. J.* **550**, 824–840.

Brandenburg, A., Svedin, A. & Vasil, G.M. 2009 Turbulent diffusion with rotation or magnetic fields. *Mon. Not. R. Astron. Soc.* **395**, 1599–1606.

Dobler, W., Stix, M. & Brandenburg, A. 2006 Magnetic field generation in fully convective rotating spheres. *Astrophys. J.* **638**, 336–347.

Frisch, U. 1995 *Turbulence*. Cambridge University Press.

Hanasoge, S.M., Duvall, T.L. & Sreenivasan, K.R. 2012 Anomalously weak solar convection. *Proc. Natl Acad. Sci. USA* **109**, 11928–11932.

Käpylä, P.J., Rheinhardt, M., Brandenburg, A. & Käpylä, M.J. 2020 Turbulent viscosity and magnetic Prandtl number from simulations of isotropically forced turbulence. *Astron. Astrophys.* **636**, A93.

Karak, B.B., Miesch, M. & Bekki, Y. 2018 Consequences of high effective Prandtl number on solar differential rotation and convective velocity. *Phys. Fluids* **30** (4), 046602.

Li, D. 2019 Turbulent Prandtl number in the atmospheric boundary layer – where are we now? *Atmos. Res.* **216**, 86–105.

O'Mara, B., Miesch, M.S., Featherstone, N.A. & Augustson, K.C. 2016 Velocity amplitudes in global convection simulations: the role of the Prandtl number and near-surface driving. *Adv. Space Res.* **58**, 1475–1489.

Ossendrijver, M. 2003 The solar dynamo. *Astron. Astrophys. Rev.* **11**, 287–367.

Pandey, A., Krasnov, D., Schumacher, J., Samtaney, R. & Sreenivasan, K.R. 2022*a* Similarities between characteristics of convective turbulence in confined and extended domains. *Physica D: Nonlinear Phenomena* **442**, 133537.

Pandey, A., Krasnov, D., Sreenivasan, K.R. & Schumacher, J. 2022*b* Convective mesoscale turbulence at very low Prandtl numbers. *J. Fluid Mech.* **948**, A23.

Pandey, A., Schumacher, J. & Sreenivasan, K.R. 2021 Non-Boussinesq convection at low Prandtl numbers relevant to the Sun. *Phys. Rev. Fluids* **6** (10), 100503.

Pencil Code Collaboration, *et al.* 2021 The Pencil Code, a modular MPI code for partial differential equations and particles: multipurpose and multiuser-maintained. *J. Open Source Softw.* **6** (58), 2807.

Rüdiger, G. 1989 *Differential Rotation and Stellar Convection. Sun and Solar-Type Stars*. Akademie Verlag.

SCHUMACHER, J. & SREENIVASAN, K.R. 2020 Colloquium: unusual dynamics of convection in the Sun. *Rev. Mod. Phys.* **92** (4), 041001.

SIEBESMA, A.P., SOARES, P.M.M. & TEIXEIRA, J. 2007 A combined eddy-diffusivity mass-flux approach for the convective boundary layer. *J. Atmos. Sci.* **64** (4), 1230–1248.

SPIEGEL, E.A. 1962 Thermal turbulence at very small Prandtl number. *J. Geophys. Res.* **67** (3), 3063–3070.

SUR, S., BRANDENBURG, A. & SUBRAMANIAN, K. 2008 Kinematic α-effect in isotropic turbulence simulations. *Mon. Not. R. Astron. Soc.* **385**, L15–L19.

TAI, N.C., CHING, E.S.C., ZWIRNER, L. & SHISHKINA, O. 2021 Heat flux in turbulent Rayleigh–Bénard convection: predictions derived from a boundary layer theory. *Phys. Rev. Fluids* **6** (3), 033501.